TISSUE ENGINEERING: Part A
Volume 00, Number 00, 2021

DOI: 10.1089/ten.tea.2020.0332

termis
Tissue Engineering
& Regenerative Medicine
International Society

Extracellular Matrix Alignment Directs Provisional Matrix Assembly and Three Dimensional Fibrous Tissue Closure

Shoshana L. Das, BS,[1–3] Prasenjit Bose, PhD,[4] Emma Lejeune, PhD,[5] Daniel H. Reich, PhD,[4] Christopher Chen, MD, PhD,[2,3] and Jeroen Eyckmans, PhD[2,3]

Gap closure is a dynamic process in wound healing, in which a wound contracts and a provisional matrix is laid down, to restore structural integrity to injured tissues. The efficiency of wound closure has been found to depend on the shape of a wound, and this shape dependence has been echoed in various *in vitro* studies. While wound shape itself appears to contribute to this effect, it remains unclear whether the alignment of the surrounding extracellular matrix (ECM) may also contribute. In this study, we investigate the role both wound curvature and ECM alignment have on gap closure in a 3D culture model of fibrous tissue. Using microfabricated flexible micropillars positioned in rectangular and octagonal arrangements, seeded 3T3 fibroblasts embedded in a collagen matrix formed microtissues with different ECM alignments. Wounding these microtissues with a microsurgical knife resulted in wounds with different shapes and curvatures that closed at different rates. Observing different regions around the wounds, we noted local wound curvature did not impact the rate of production of provisional fibronectin matrix assembled by the fibroblasts. Instead, the rate of provisional matrix assembly was lowest emerging from regions of high fibronectin alignment and highest in the areas of low matrix alignment. Our data suggest that the underlying ECM structure affects the shape of the wound as well as the ability of fibroblasts to build provisional matrix, an important step in the process of tissue closure and restoration of tissue architecture. The study highlights an important interplay between ECM alignment, wound shape, and tissue healing that has not been previously recognized and may inform approaches to engineer tissues.

Keywords: provisional matrix assembly, fibronectin, ECM alignment, wound closure, tissue repair

Impact Statement

Current models of tissue growth have identified a role for curvature in driving provisional matrix assembly. However, most tissue repair occurs in fibrous tissues with different levels of extracellular matrix (ECM) alignment. Here, we show how this underlying ECM alignment may affect the ability of fibroblasts to build new provisional matrix, with implications for *in vivo* wound healing and providing insight for engineering of new tissues.

Introduction

The assembly of provisional matrix is a critical step in wound closure and the formation of tissue *de novo*. During the repair of full-thickness wounds, fibroblasts first migrate into the wound area and deposit extracellular matrix (ECM) proteins such as fibronectin. These proteins serve as a template for other cell types, including endothelial cells and immune cells to migrate on.[1–4] Later, epithelial cells use this provisional matrix or granulation tissue as a substrate to migrate over and cover the wound bed to complete closure.[5–7]

While it has been reported that insufficient or delayed formation of granulation tissue can lead to impaired gap closure and delayed reepithelialization,[7,8] the factors that

[1]Harvard-MIT Program in Health Sciences and Technology, Institute for Medical Engineering and Science, Massachusetts Institute of Technology, Cambridge, Massachusetts, USA.
[2]Department of Biomedical Engineering, Boston University, Boston, Massachusetts, USA.
[3]Wyss Institute for Biologically Inspired Engineering, Harvard University, Boston, Massachusetts, USA.
[4]Department of Physics and Astronomy, Johns Hopkins University, Baltimore, Maryland, USA.
[5]Department of Mechanical Engineering, Boston University, Boston, Massachusetts, USA.

drive the rate of granulation tissue formation remain elusive. Understanding how to modulate this rate of tissue assembly is not only important in the context of wound healing but also in the biomanufacturing of engineered tissues.

In clinical settings, wound closure rates correlate with the shape of a wound, an observation that has been echoed in several studies of reepithelization.[9–11] For example, in epithelial monolayers, prepatterned gaps with concave shapes close faster compared to those with convex shapes.[12,13] The increased rate of closure in regions of high curvature stems from the emergence of contractile actomyosin rings spanning multiple epithelial cells that pull the wound margins closer.[14–16]

Curvature has also been suggested to control new matrix formation by fibroblasts, which lack these multicellular contractile rings, in models of tissue growth into pores.[17–19] More recently, it has been shown that minimization of surface tension developed by cell contractility drives the kinetics of curvature-mediated tissue growth.[20] A similar mechanism has been proposed to explain wound closure in collagenous microtissues, wherein minimization of surface stresses emerging from contractile cells that are adherent to fibronectin matrix at the surface of the microtissue drive the flow of cells and fibronectin in the gap.[21]

While curvature of the wound edge has been associated with wound closure rates, wound shape and healing rate are also dependent on the local organization of the underlying ECM. For example, in surgical settings, incisions made across the natural orientation of collagen fibers in the dermis results in wide open gaps that heal poorly, whereas by cutting along the direction of natural ECM alignment, incisions gape less, leading to faster healing and less scarring.[10,22] Although the mechanism underlying this clinical practice is not well understood, there is a clear evidence that ECM alignment guides migratory and contractile processes of fibroblasts that are crucial for wound closure.[23–26] However, how this ECM alignment and curvature affect the assembly of new tissue, such as granulation tissue or the generation of new tissue, remains to be explored.

To study how curvature and ECM alignment may influence tissue closure by fibroblasts, we use a previously established model of 3D stromal gap closure, wherein fibroblasts in engineered collagen-based microtissues[27] are injured and then assemble a provisional fibronectin template to close the gap. Here, we use an approach to change the shape of the microtissues, to either rectangular or octagonal, to affect the alignment of the ECM,[28,29] and show that ECM alignment may locally act as a negative regulator of provisional matrix assembly and thus modulating the rate of new tissue formation.

Materials and Methods

Cell preparation and culture

NIH 3T3 cells (ATCC) were maintained in high glucose DMEM (Corning) containing 10% Bovine Serum and 1% Penicillin Streptomycin solution (Gibco). Cells were used between passages 5 and 15.

Microtissue seeding

Rectangular and octagonal microtissues were prepared as previously described.[28,30] In brief, polydimethylsiloxane microfabricated tissue gauges (μTUGs) were prepared by molding from SU-8 masters.[28,30] μTUG devices were UV sterilized, then treated with 0.02% Pluronic F127 (Sigma) for 15 min to prevent cell and extracellular attachments. 3T3 cells were dissociated from cell culture plates, suspended in a 2 mg/mL Collagen I, Rat Tail (Corning) hydrogel solution at a concentration of 1 million/mL, and maintained on ice to prevent polymerization. Cell suspensions were centrifuged at −9°C into devices, and excess was removed before polymerization at 37°C for 10 min. Microtissues were maintained in high-glucose DMEM containing 10% bovine serum and 1% penicillin streptomycin solution.

To visualize collagen matrix of microtissues, 5% (w/w) Alexa Fluor 555 conjugated Collagen I (Thermo Fisher) was added to the cell suspension before device seeding. To visualize fibronectin matrix within microtissues, 8 μg/mL of Alexa Fluor 488 (Thermo Fisher) conjugated human fibronectin (isolated from human plasma) was added to media during the first 24 h of tissue formation.

Twenty-four hours after devices were seeded, a diamond dissecting knife (type MDL, Electron Microscopy Systems, #72029) mounted on a XYZ micromanipulator (SLC-2040, SmarAct GmbH) was used to create full-thickness incisions in the centers of the microtissues by making cuts layer-by-layer at increasing depths using a microscope for visual feedback. Incisions were oriented from top to bottom. The ranges for incision length were 14–30% for rectangles and 17–34% for octagons as a percent of the total length of the tissue along the incision orientation.

Time-lapse microscopy and closure rate measurements

For wide-field time-lapse imaging, phase contrast and fluorescent images were captured every 30 min for over 16–20 h. Tissues were exposed every 30 min to a 33–50 ms exposure for brightfield, and a 150–300 ms exposure in the fluorescent channels. They were recorded with a Photometrics Evolve 16-bit electron-multiplying CCD camera (Photometrics) and an A-Plan 10× objective mounted on a Nikon Ti Eclipse (Nikon Instruments, Inc.) microscope maintained at 37°C at 5% CO_2.

Phase contrast images were used to measure gap area every 2 h over the indicated time, and closure rates were calculated using the slope from a Least Squares Regression Line that was fitted through the data for each individual tissue. The data were truncated if closure completed before the indicated time, or if the tissue ruptured or tore. Ellipsoidal shapes were fitted to the wound boundaries in ImageJ. The major and minor axes of these ellipses were used to parametrize the wounds' shapes, and the ellipses were also used for calculations of the wounds' curvature and eccentricity.

Confocal microscopy

To visualize ECM, microtissues with Alexa 555-tagged collagen and Alexa 488 fibronectin were imaged on a Leica SP8 confocal microscope with a Leica 40× water objective and Leica LAS X imaging software. For fiber analysis, z stacks of microtissues with Alexa 488-tagged fibronectin were imaged on a Yokogawa CSU-21-Zeiss Axiovert 200M inverted spinning-disk microscope with a Zeiss 40× water objective and Evolve EMCCD camera (Photometrics).

ImageJ and the Pairwise Stitching plugin[31] were used to stitch images together and then maximum projections were used for analysis.

Fiber analysis

Analysis of fibronectin fibers was performed using an established MATLAB code[28] based on the FibrilTool method[32] to measure fiber orientation and anisotropy. In brief, first, a Gaussian blur function was applied to images to reduce pixelation effects, then for every pixel in selected region, the local pixel intensity gradient was used to determine a perpendicular normalized vector and then this was used to calculate the local nematic tensor for each pixel.

The region was then subdivided into 5 pixel $\times$ 5 pixel squares and the average nematic tensor for each subregion was calculated. The largest eigenvector corresponding to the largest eigenvalue (λ_1) of this average describes the alignment direction, and the difference of the two eigenvalues ($q = \lambda_1 - \lambda_2$) defined the anisotropy of each region. These were then averaged for each $30 \times 30\,\mu m^2$ regions tangent to the top and side edge of the bulk tissue adjacent to the wound edge.

Computational model

Computational modeling was performed using FEniCS,[33,34] an open source finite element analysis computing platform. The microtissue was approximated as a random fiber network, where fibers represent ECM fibers. The random fiber network finite element mesh was initialized with the Gmsh mesh generator.[35] Each domain contained $\sim$1100–1400 fibers of length 100 μm with initial fiber angle sampled from a uniform distribution.

In the rectangular geometry, a 10 μm by 300 μm rectangular wound was initialized in the center of the domain. In the octagonal geometry, a 10 μm by 150 μm rectangular wound was initialized in the center of the domain. In both domains, the micropillar attachment sites were simulated as Dirichlet boundary conditions. The microtissue fibers were approximated as a homogeneously contracting Neo-Hookean material where homogeneous volumetric contraction was applied up to a dimensionless shrinkage of 0.6 following the standard multiplicative decomposition model for biological tissue growth (and shrinkage).[36]

Geometry set up and subsequent simulation analysis and plotting were performed with Python,[37] Numpy,[38] and Matplotlib.[39] Further details of the model are included in the Supplementary Data under Description of Fiber Model. For postprocessing, anisotropy was computed directly from the deformed geometry of the finite element mesh[32] using 50 μm square ROIs adjacent to the wound edge. To account for the effect of different random fiber distributions, one hundred simulations were performed and analyzed for each geometry.

Statistical analyses

Two-tailed Student's *t*-tests were used for all statistical analyses. For statistical comparisons within the same tissue, a paired *t*-test was used, while between different tissues, an unpaired *t*-test was used. Significant values are indicated as $*p \le 0.05$, $**p \le 0.01$, $***p \le 0.001$.

Results

Closure of elliptical gaps in fibrous microtissues

To investigate fibrous tissue closure in highly aligned matrices, we generated microtissues composed of NIH 3T3 fibroblasts in a collagen type I matrix formed around flexible polydimethylsiloxane (PDMS) pillars that were spaced in a rectangular pattern with a 4 to 1 aspect ratio[28] (Fig. 1a). After the tissue was compacted around the pillars (18–24 h after seeding), an incision was cut in the center of the tissue using a microdissection knife. Upon injury, the incision opened to form an elliptical shaped gap (Fig. 1b, left). Over the next 20 h, this gap spontaneously closed in a linear manner (Fig. 1b, c) with a constant rate of change in gap area of $-627 \pm 34\,\mu m^2/h$ (mean ± SEM) (Fig. 1c and Supplementary Video S1) and had a slight increase in eccentricity between the start and 10 h into healing from 0.958 ± 0.003 to 0.968 ± 0.003 (mean ± SEM, $p = 3.0 \times 10^{-4}$, Fig. 1d).

To investigate how the elongated shape of the tissue and elliptical gap affect the dynamics of tissue closure, we measured the change in length of the major and minor axes of the gap over time and calculated their rates of change. We found that closure rate of the major axis was 9.3 ± 0.7 μm/h (mean ± SEM), 3.4 × faster than the closure rate of the minor axis (2.7 ± 0.1 μm/h, mean ± SEM, $p = 1.1 \times 10^{-12}$, Fig. 1e, f). These data suggest that tissues' geometric boundary conditions dictate the gap closure process, with significantly faster closure rates along the major axis.

Assembly of fibronectin template occurs primarily along the major axis and is not correlated with the curvature of the wound edge

As previously described in Selman Sakar *et al*,[27] gap closure in this model system is driven by two mechanisms: contractility-dependent compaction and the building of new provisional fibronectin matrix that fills the gap (Fig. 2a). To visualize these two processes, fluorescently labeled collagen and fibronectin were added during tissue formation and imaged hourly throughout the healing process. At high magnification (40×), fluorescently labeled collagen and fibronectin were seen in the bulk tissue. Fibronectin populated with cells was also observed within the gap, showing the provisional matrix assembled by cells during closure (Fig. 2b, top).

Since the field of view was limited at high magnification, we explored whether the provisional matrix could be visualized at lower magnification (10×) to enable quantification of compaction and provisional matrix assembly using images that show the tissue in a larger field of view. At this magnification, the fluorescent signal from fibronectin and collagen in the bulk tissue overlapped, but the faint fibronectin signal from the provisional matrix was not detectable (Fig. 2b, bottom). Due to this limitation, we used brightfield images as a proxy for total closure instead, and subtracted these images from the fluorescent images showing the bulk tissue.

At this magnification, the area of new provisional matrix deposition was identified as new material visible by phase but not detectable in the fluorescent imaging (Fig. 2c). Thus, the boundaries for these regions could be calculated (Fig. 2c, yellow dotted line bounding the fluorescently tagged collagen; green region showing area of new provisional matrix). Using this method, we tracked compaction of the original

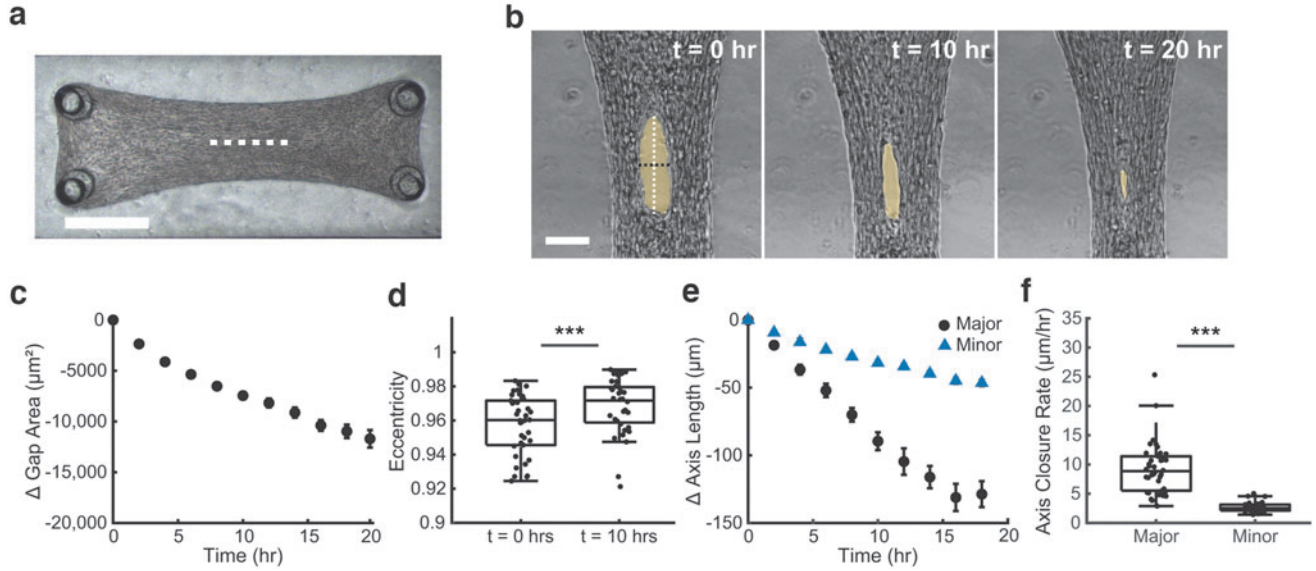

FIG. 1. Closure of elliptical gaps in fibrous microtissues. **(a)** NIH 3T3 microtissue 24 h postseeding, before injury. *White dashed line* indicates orientation of incision. (Scale bar = 300 μm). **(b)** Injured microtissue spontaneously closing over time at 0, 10, and 20 h postinjury (Scale bar = 100 μm). *Yellow* regions indicate open gap. *White* and *black dashed lines* indicate major and minor axes, respectively. **(c)** Change in gap area over time, averaged over three separate experiments ($n = 38$ tissues). **(d)** Eccentricity of open gap after injury and 10 h into healing, $***p < 0.001$, $n = 36$ tissues. **(e)** Change in major (*black circles*) and minor (*blue triangles*) axis length of gap over time ($n = 38$ tissues). **(f)** Linear rate of axes change throughout closure process, $***p < 0.001$, $n = 38$ tissues. Box plots represent 25th–75th percentiles, with *whiskers* extending 1.5 × the interquartile range and *horizontal lines* showing the medians.

tissue boundary and new provisional matrix over time (Fig. 2d, e). Given the differences in major and minor axis closure rates previously observed, we also compared the rates of compaction and new matrix assembly specifically in these regions (Fig. 2f).

The total axis closure rate was significantly different between the major and minor axes, 19.1 ± 1.0 μm/h and 4.1 ± 0.2 μm/h, respectively (mean ± SEM, $p = 1.2 \times 10^{-7}$). We note these rates are higher than in Figure 1f, we believe that this may be a result of the addition of the tagged fibronectin during the formation process. Separating the contributions from compaction and fibronectin matrix growth, we observed that while compaction between both axes was not significantly different (Major: 4.2 ± 0.9 μm/h, Minor: 2.6 ± 0.2 μm/h, mean ± SEM, $p = 0.074$), fibronectin matrix growth was higher in the major axis compared to the minor axis (Major: 14.9 ± 0.9 μm/h, Minor: 1.6 ± 0.2 μm/h, mean ± SEM, $p = 2.5 \times 10^{-7}$).

These data suggest that the difference seen in total closure was due to regional differences in provisional matrix, rather than compaction of the tissue. Therefore, moving forward, we focused on understanding the drivers for differential growth of the fibronectin matrix in our model system.

As studies have highlighted the role of curvature on the rate of provisional matrix growth,[17–20] we investigated if curvature could be used to explain the rates found in this model. Since the point of maximum curvature occurs where the major axis crosses the wound edge, we analyzed the curvature and the provisional matrix growth over time in this region, heretofore referred to as ''Top'' (Fig. 2g).

FIG. 2. Assembly of fibronectin template occurs primarily along the major axis and is not correlated with the curvature of the wound edge. **(a)** Schematic of contributions of both tissue compaction and provisional fibronectin matrix to closure process. **(b)** Tissue at 10 h postinjury labeled with Collagen-Alexa 555 (*magenta*), Fn-Alexa 488 (*green*), nuclei (cyan) at 40 × confocal (*top*, scale bar = 25 μm) and 10 × Widefield (*bottom*, scale bar = 100 μm). *Dashed yellow line* indicates the inner tissue boundary. *White dashed* box indicates 40 × field of view. **(c)** Widefield image of microtissues 10 h postinjury. Brightfield (*top*) with *yellow* region indicating open gap. Collagen-Alexa 555 (*middle*) and Fn-Alexa 488 (*bottom*) with *yellow* region overlaid. *Dashed yellow line* indicates inner tissue boundary, *green* region indicates provisional fibronectin matrix. **(d)** Widefield imaging of tissue with FN-Alexa 488 after injury at $t = 0$, 10, and 20 h. Brightfield (*top*) with *yellow* region indicating total gap, Fn-Alexa 488 (*bottom*), with *yellow* region overlaid. *Dashed yellow line* indicates inner tissue boundary, *green* region indicates provisional fibronectin matrix. **(e)** Change in gap area over time; total (*black circles*) broken down into the contribution of compaction (*blue triangles*) and fibronectin provisional matrix (*green squares*) ($n = 10$). **(f)** Major and minor axes linear closure rates broken down into the contribution of compaction and fibronectin, $***p < 0.001$, *ns*: $p > 0.05$, $n = 10$. Box plots represent 25th–75th percentiles, with *whiskers* extending 1.5 × the interquartile range and *horizontal lines* showing the medians. **(g)** Maximum curvature of gap over time (*left axis*, *black circles*, *Least Squares* Regression Line: $y = 0.029x + 0.05$, $R^2 = 0.98$) and provisional matrix growth rate at point of maximum curvature over time (*right axis*, *gray squares*, *Least Squares* Regression Line: $y = 0.1082x + 11.27$, $R^2 = 0.0067$).

Over the course of closure, curvature increased at a rate of $0.29\,\mu m^{-1}h^{-1}$ (from Least Squares Regression Line: $y = 0.029x + 0.05$, $R^2 = 0.98$), while the rate of provisional matrix growth from the point of maximum curvature remained constant. Given this weak correlation between curvature and provisional fibronectin matrix growth, we set out to investigate other parameters that may explain the axial difference in assembly of the provisional fibronectin matrix in this model of tissue closure.

Local fibronectin alignment at gap edge correlates with the assembly of fibronectin provisional matrix

Given that fibroblast–fibronectin interactions are critical for closure in this model system,[27] we tested whether ECM alignment is correlated with the deposition of provisional matrix in the gap area. Using a MATLAB code developed based on the FibrilTool algorithm,[28,32] we measured fiber orientation and anisotropy (degree of alignment), in the Top

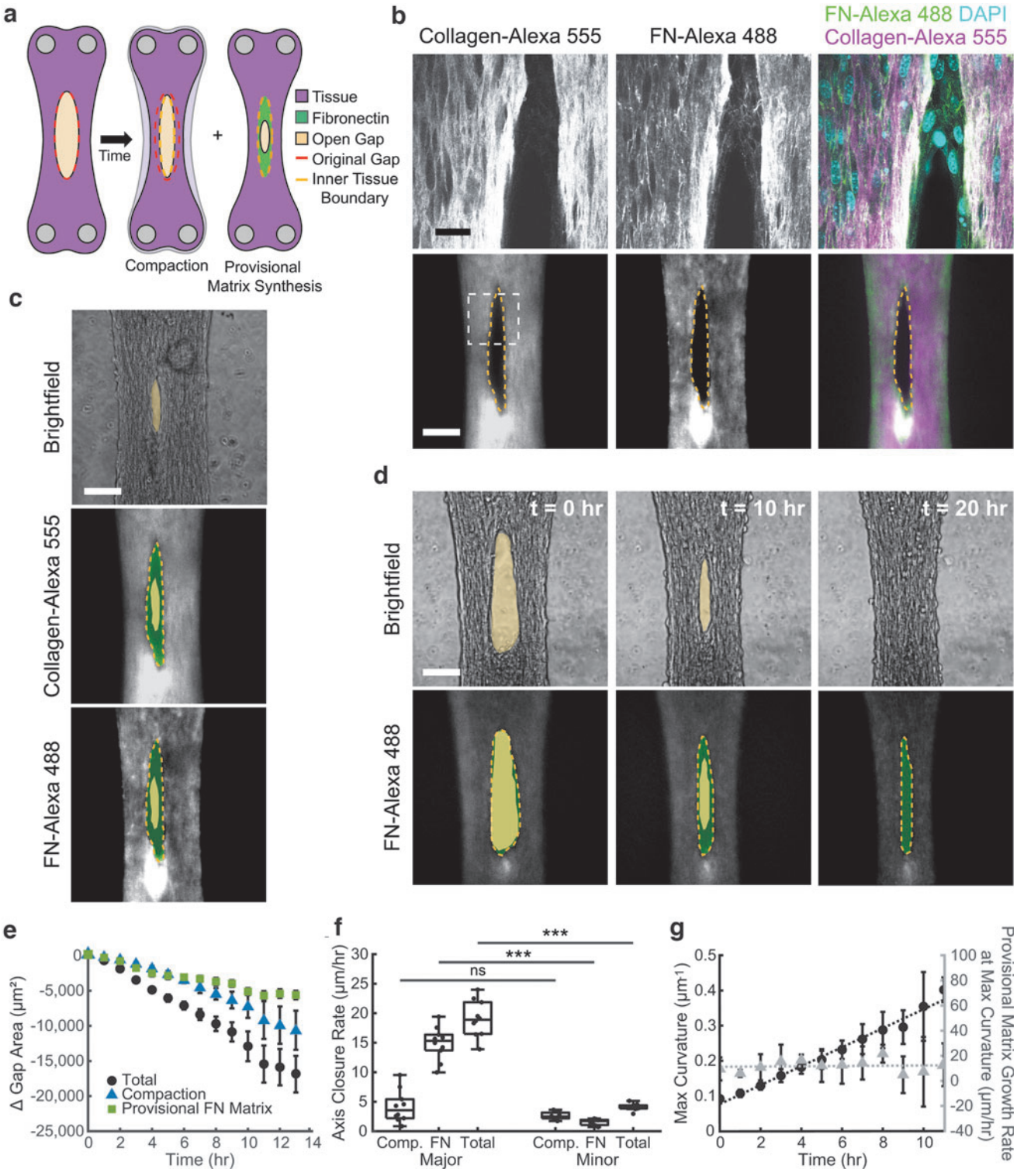

region and the region where the minor axis crosses the wound edge (heretofore referred to as the "Side" of the wound). Due to artifacts from excess tissue material from the incision (Fig. 3a, white arrowhead), only the top edge and one side of the gap were analyzed. For both regions, 0° is defined as the tangent line to the wound edge for the angle of orientation measurements.

Fibronectin fibers were oriented parallel to the wound edge in the side regions, whereas fibronectin fibers in the top regions were oriented perpendicular to the wound edge (Fig. 3b). The anisotropy of the fibrous matrix was significantly ($p=0.036$) lower in the top regions (0.19 ± 0.02, mean ± SEM) compared to the side regions (0.26 ± 0.05, mean ± SEM, Fig. 3c). Together, these data demonstrate that fibronectin fibers are more aligned at the side edge of the wound compared to the top edge.

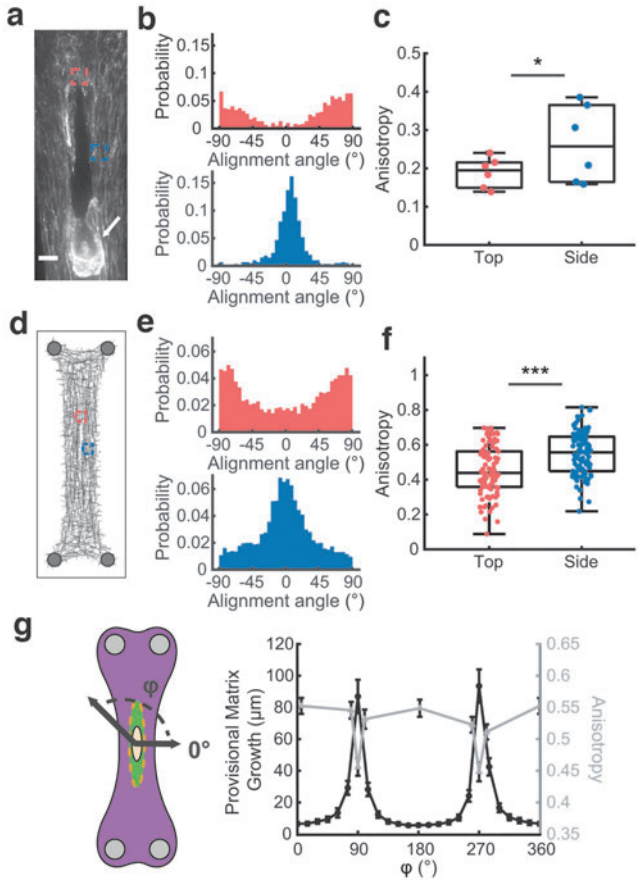

FIG. 3. Local fibronectin alignment at gap edge correlates with the assembly of fibronectin provisional matrix. **(a)** Maximum projection of tissue (40×) with Fn-Alexa 488, fixed 10 h postinjury (Scale bar = 30 μm). Regions of analysis (30×30 μm) and orientations for fibronectin fiber alignment angle and anisotropy **(b, c)** are shown for *Top* (*red*) and *Side* (*blue*) edges. *White arrow* indicates excess tissue from incision. **(b)** Alignment angle for corresponding regions: *top* (*top*) *side* (*bottom*) shown in **(a)** ($n=6$). **(c)** Average anisotropy for regions shown in **(a)**, $*p<0.05$, $n=6$. **(d)** Computational model of injured tissue. Regions of analysis (50×50 μm) are shown for *top* (*red*) and *side* (*blue*) edges. **(e)** Fiber alignment angle for regions specified in **(d)** for 100 simulations. **(f)** Average fiber anisotropy in regions specified in **(d)** for 100 simulations, $***p<0.001$. **(g)** Radial provisional matrix length at 10 h (from experimental data, *left axis*, *black circles*) and fiber anisotropy for 8 regions (50 μm by 50 μm) around gap from 100 simulations of model (*right axis*, *gray triangle*). The width of bins for histograms in **(b, e)** is 5°. Box plots represent 25th–75th percentiles, with *whiskers* extending 1.5× the interquartile range, and horizontal lines represent medians.

To understand how fiber alignment and orientation are fundamentally linked to the tissue shape, we built a computational model of ECM fibers using the Finite Element Method[36] (Supplementary Figs. S1 and S2). In the stress-free reference configuration, we initialize randomly oriented ECM fibers. Then, we applied homogeneous contraction to simulate how cells enact mechanical forces onto ECM and observed how ECM fiber alignment emerged in the deformed configuration due to the interaction between tissue contraction, tissue geometry, and boundary conditions.

A similar fiber analysis as described above for the microtissues was performed for 100 simulations of the model. Confirming our experimental findings, the simulations showed an increased fiber anisotropy at the side of the gap compared to the top (Anisotropy: Top: 0.46 ± 0.01, Side: 0.55 ± 0.01, mean ± SEM, $p=3.3\times10^{-7}$, Fig. 3e, f). Not only do these findings validate the computational model but they also suggest that contractility is sufficient to model ECM alignment in our system.

To determine the relationship between fiber anisotropy and provisional matrix growth, we plotted provisional matrix length at 10 h as a proxy for provisional matrix growth (derived from experimental data, Fig. 2d) and local tissue anisotropy (from computational model) as a function of angle around the gap (Fig. 3g). Interestingly, regions with lower fiber anisotropy showed more provisional matrix growth compared to regions with high-fiber anisotropy, therefore, suggesting that provisional matrix assembly in the gap is inversely correlated to how aligned the ECM of the adjacent tissue is.

Octagonal tissues with reduced matrix alignment exhibit greater and more uniform fibronectin growth around the gap

To elaborate further the hypothesis that ECM anisotropy affects provisional matrix assembly, we investigated wound closure in octagonal microtissues which have an isotropic fiber alignment[28] (Fig. 4a). Upon incision, the gap opened up in a more circular shape compared to the highly elliptical shape in the rectangular tissues (Fig. 4b), and closed spontaneously (Fig. 4c and Supplementary Video S2). As with the rectangular tissues, we measured the closure rates of the gap axes over time (Fig. 4d). Having established a wound closure model in isotropic microtissues, we investigated the contribution of compaction and provisional matrix assembly along the horizontal and vertical axes.

In contrast to the rectangular microtissues, the horizontal axis closed slightly faster than the vertical axis, 9.1 ± 0.9 and 7.8 ± 0.6 μm/h, respectively (mean ± SEM, $p=4.9\times10^{-3}$, Fig. 3e). Both compaction and provisional fibronectin matrix growth were significantly different between both axes, but overall, the differences were much subtler than in the rectangular tissues (Compaction: Horizontal: 2.8 ± 0.3 μm/h, Vertical: 3.8 ± 0.6 μm/h, mean ± SEM, $p=0.042$, Fibronectin: Horizontal: 6.3 ± 0.8 μm/h, Vertical: 4.0 ± 0.4 μm/h, mean ± SEM, $p=2.3\times10^{-3}$). These differences are caused by the cutting direction, because our method of cutting resulted in

accumulation of tissue at the end of the incision compared to the edges and the linear nature of the incision and how it opens both introduced anisotropy into the system.

As anticipated, the orientation of the fibronectin fibers and anisotropy was not as different when comparing the top and side edges of wounds (Fig. 4f–h). Although initially oriented isotropically,[28] fibronectin fibers tend to align parallel to the wound edge after injury (Fig. 4g) with similar anisotropy values for top (0.17 ± 0.01, mean ± SEM) and side regions (0.19 ± 0.02, mean ± SEM, $p = 0.27$, Fig. 4h).

The rearrangement of fibers at the wound edge was also captured by the computational model (Fig. 4i) with the top and sides having similar fiber orientations both parallel to the wound edge (Fig. 4j). In contrast to the experimental model, the computational model predicted a slightly different fiber anisotropy between the top and side regions, 0.37 ± 0.01 and 0.42 ± 0.01, respectively (mean ± SEM, $p = 5.0 \times 10^{-5}$, Fig. 4k). However, these anisotropies were both lower than the Side region of the rectangular tissues (Top of octagon to side of rectangle: $p = 1.6 \times 10^{-20}$, Side of octagon to side of rectangle: $p = 5.3 \times 10^{-11}$).

To investigate if local ECM anisotropy was also inversely correlated with provisional matrix assembly in octagonal microtissues, provisional matrix length for tissues 10 h into healing was plotted vs position around the wound along with fibronectin anisotropy from the model (Fig. 4l). Unlike rectangular tissues where the length of the provisional template spiked adjacent to regions with low anisotropy, the length of the provisional matrix in octagonal microtissues was more uniform around the gap, with only a drop at 270° corresponding to the bottom of the incision where excess ECM from the incision was present.

Given that the assembly of a fibronectin template occurred uniformly around the gap in octagonal tissues and predominately along the long axis in rectangular tissues, we hypothesized that gap closure depends on the overall tissue geometry. Indeed, in a side-by-side comparison, wounds in octagonal tissues showed higher total area of provisional matrix at 10 h into the healing, $8330 \pm 710\ \mu m^2$ versus $5730 \pm 926\ \mu m^2$ (mean ± SEM, $p = 0.029$, Fig. 4m). To compare closure rates, we used the closure rate for the first 10 h, since after this time point closure slowed down in octagon tissues (Fig. 4c). Octagons ($1400 \pm 120\ \mu m^2$/h) had almost double the closure rate of rectangles ($750 \pm 49\ \mu m^2$/h, mean ± SEM, $p = 1.5 \times 10^{-7}$, Fig. 4n).

While confounding factors such as mechanical constraints and surface tension could be contributing, these data suggest that the lower alignment found in the octagonal tissues is associated with more provisional matrix assembly and overall faster healing rates compared to the rectangular tissues, where highly aligned edges may have impaired the assembly of new provisional matrix.

Discussion

Clinical observations and early studies in rabbit models have shown that wound shape is a critical determinant for closure.[9–11,22] To understand how wound shape affects the cellular and mechanical mechanisms underlying tissue repair, bioengineered *in vitro* models have been developed wherein gaps with different shapes are patterned in epithelial monolayers using stamping techniques[12,13] or cut with laser light.[40] Recently, 3D scaffolds were used to study tissue growth under tension[20] and fabricated microcontainers with different shapes have been used to study gap closure in 3D.[41]

While these methods directly control gap geometry, our model system controls wound shape by changing the overall tissue geometry. Thus, similar to cuts in patients, the shape of the gap in our model system depends on the prestress of the tissue matrix, which enables studies of the effects of tissue properties surrounding the wound on gap closure *in vitro*.

Another unique feature of this biomimetic *in vitro* wound healing model is that closure is strongly dependent on the assembly of a provisional fibronectin template.[27] Assembly of provisional fibronectin matrices has also been described in pore filling models.[17,18] In pores with different geometries, fibroblasts first assemble provisional matrix to make gaps circular before proceeding to fill the gap uniformly. This observation has led to the idea that minimizing surface tension, and as such minimizing curvature, drives the growth of fibronectin matrices in pores with different geometries.[17,20,42]

While minimizing surface tension has also been suggested to drive gap closure in fibrous microtissues,[21] our study shows that during healing, the eccentricity of the gaps and fibronectin tissue growth in rectangular microtissues remains relatively constant whereas curvature increases. Thus, our data suggest that other factors, such as ECM alignment, may

FIG. 4. Octagonal tissues with reduced matrix alignment exhibit greater and more uniform fibronectin growth around the gap. **(a)** Octagonal microtissue 24 h postseeding, before injury (Scale bar = 300 μm). *White dashed line* indicates orientation of incision. **(b)** Injured microtissue spontaneously closing over time at 0, 10, and 20 h postinjury (Scale bar = 100 μm). *Yellow region* indicates open gap. *White* and *black dashed lines* indicate vertical and horizontal axes, respectively. **(c)** Change in gap area over time for three separate experiments ($n = 27$ tissues) **(d)** Change in *vertical* (*black circles*) and *horizontal* (*blue triangles*) *axis* length of gap over time ($n = 27$ tissues). **(e)** Major and minor axes linear closure rates broken down into the contribution of compaction and fibronectin, $^{**}p < 0.01$, $^{*}p < 0.05$, $n = 10$. **(f)** Maximum projection of tissue (40×) with Fn-Alexa 488, fixed 10 h postinjury. Regions of analysis (30 × 30 μm) and orientations for fibronectin fiber alignment angle and anisotropy **(g, h)** are shown for *top* (*red*) and *side* (*blue*) edges. (Scale bar = 30 μm) **(g)** Alignment angle for corresponding regions: *top* (*top*) and *side* (*bottom*) shown in Figure 4f ($n = 6$). **(h)** Average anisotropy for regions shown in **(f)**, *ns*: $p > 0.05$, $n = 6$. **(i)** Computational model of injured tissue. Regions of analysis (50 × 50 μm) are shown for *top* (*red*) and *side* (*blue*) edges. **(j)** Fiber alignment angle for regions specified in **(i)** for 100 simulations. **(k)** Average fiber anisotropy in regions specified in **(i)** for 100 simulations, $^{***}p < 0.001$. **(l)** Radial provisional matrix length at 10 h (from experimental data, *left axis*, *black circles*) and fiber anisotropy for eight regions (50 μm by 50 μm) around gap from 100 simulations of model (*right axis*, *gray triangle*). **(m)** Provisional matrix area at 10 h for rectangular and octagonal tissues, $^{*}p < 0.05$ ($n = 9$, 10). **(n)** Closure rates for the first 10 h for rectangular and octagonal tissues, $^{***}p < 0.001$ ($n = 38$, 27). The width of bins for histograms in **(g, j)** is 5°. Box plots represent 25th–75th percentiles, with *whiskers* extending 1.5 × the interquartile range, *horizontal line* represents median.

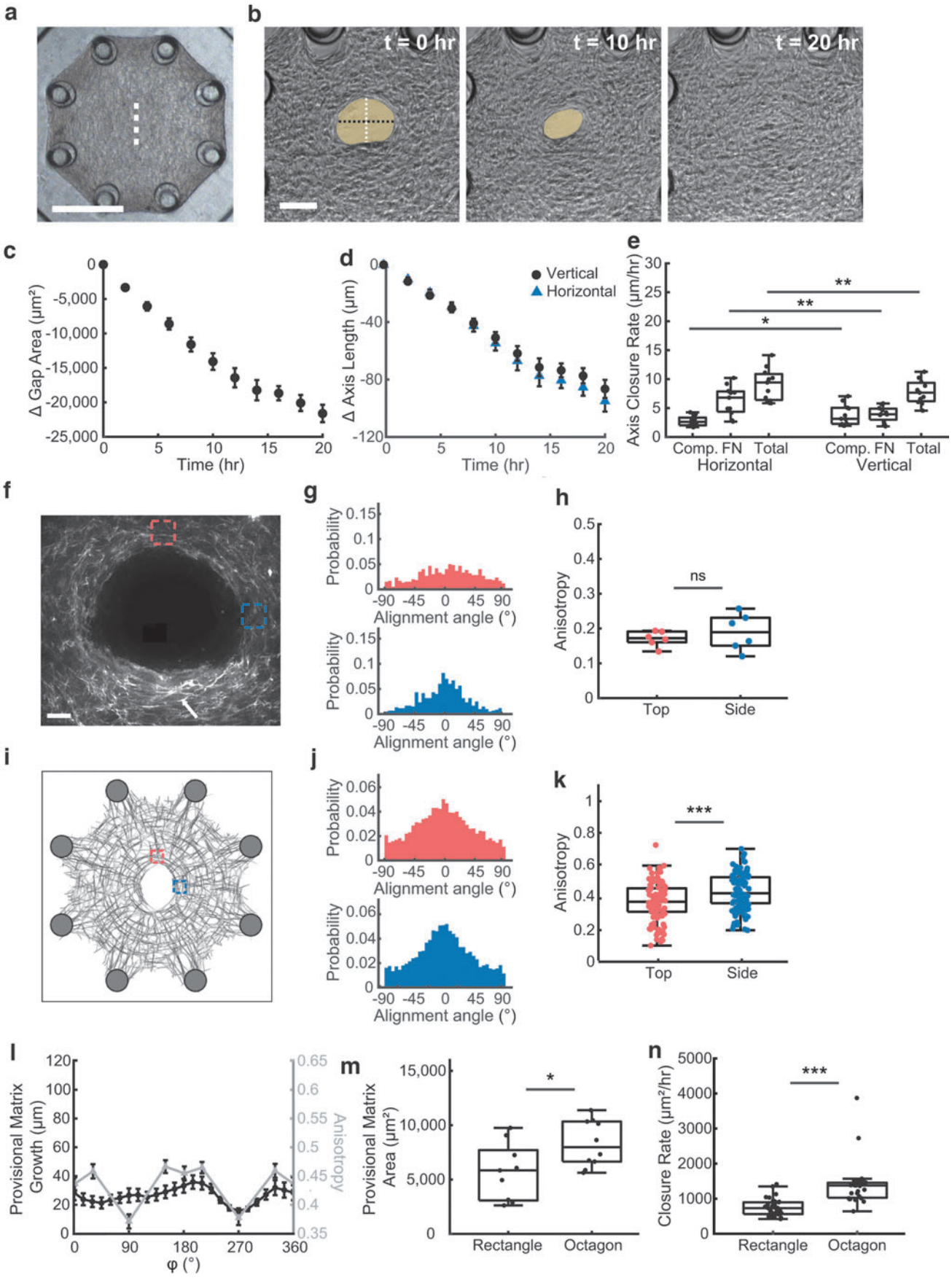

add an additional layer of regulation to provisional matrix assembly and gap closure.

While this study reveals a correlation between ECM alignment and provisional matrix growth in gap closure, the impaired provisional matrix growth along the highly aligned edges of rectangular microtissues could be explained by multiple causes. ECM fibers can provide topological cues to direct cell migration along the aligned fibers,[25,26,43–45] therefore hindering cells from moving into the gap. Conversely, cells can migrate randomly in less aligned ECMs, as observed in the top region of gaps in rectangular microtissues and in octagonal microtissues, which may facilitate movement into the gap.

Alternatively, matrix alignment is inherently linked to augmented tissue stress that is transmitted through the ECM.[46–48] These stresses have been shown to alter the conformation and state of individual fibronectin fibers.[49] While stretch is required for fibrillogenesis, highly stretched fibronectin shows reduced colocalization to other ECM molecules such as collagen type I,[50] which may hamper assembly and ingrowth of a provisional matrix. Given the intricate relationships between ECM alignment, contractility, and tissue stress, parsing out the contribution of each factor separately will be a challenging task. Nevertheless, such mechanistic studies are needed to understand how increased ECM alignment affects the assembly of a provisional matrix in wounds.

Computational models are powerful tools to parse out the effect of multiple factors on wound closure. In this study, we used a mechanical fiber model to gain insight in how contractility of the ECM affects ECM alignment after injury. The model predicted the opening of the wound as well as the fiber rearrangement at the wound margin. Interestingly, the model also predicted slightly different anisotropy values for side versus top regions in both rectangular and octagonal tissues, a finding that was not confirmed experimentally in the case of the octagonal tissues. This was predicted in the model because an anisotropic wound was initialized.

We note that in our computational model, the gaping of the wound does differ from the experimental findings. This is due to limitations in the model which does not consider crosslinking, breaking, and reforming of ECM fibers. Therefore, unlike the experimental model system, the computational model does not account for stress relaxation caused by tissue remodeling and viscoelastic properties of the collagen gel. We anticipate that this simplification is the major source of inconsistency between the computational model and experiments. However, there were some differences in overall healing and the contribution of compaction and provisional matrix assembly between the two axes of octagonal tissues.

Given the overall symmetry of octagonal microtissues, such differences, although modest, were unexpected. We speculate that asymmetry in the closure may be associated with the mode of injury. In our experiments, an incision from top to bottom was made with a microdissection knife, and in this process, ruptured tissue accumulated at the bottom side of the tissue may have affected the closure process.

Conclusion

Using a bioengineered model system, we present here a novel *in vitro* approach to investigate the role of ECM alignment on wound shape and provisional matrix assembly. Our study suggests that ECM alignment can limit the assembly of a provisional template. Harnessing this principle of tissue growth may one day suggest treatments to disrupt local ECM alignment *in situ* as a mechanism to improve healing of highly aligned tissues such as tendons and ligaments, or inform new strategies to direct ECM assembly in tissue engineering applications.

Acknowledgments

We thank Prof. Michael Smith and Dr. Tommaso Ristori for their input and technical expertise. We thank Amy Zhong and Lori Luo for helping with device fabrication. We also thank Megan Griebel and Connie Chan for contributions that did not end up in the final work.

Disclosure Statement

The authors declare no competing financial interests.

Funding Information

S.L.D. acknowledges funding from the National Science Foundation Graduate Research Fellowship.

(1122374). This work was supported by NIBIB (R21 EB028491) and NSF Grants CMMI-1463011 at JHU and CMMI-1462710 at BU.

Supplemental Material

Supplementary Data
Supplementary Figure S1
Supplementary Figure S2
Supplemental Video S1
Supplemental Video S2

References

1. Clark, R.A.F., Lanigan, J.M., DellaPelle, P., Manseau, E., Dvorak, H.F., and Colvin, R.B. Fibronectin and fibrin provide a provisional matrix for epidermal cell migration during wound reepithelialization. J Invest Dermatol **79,** 264, 1982.
2. Greiling, D., and Clark, R.A.F. Fibronectin provides a conduit for fibroblast transmigration from collagenous stroma into fibrin clot provisional matrix. J Cell Sci **110,** 861, 1997.
3. Barker, T.H., and Engler, A.J. The provisional matrix: setting the stage for tissue repair outcomes. Matrix Biol **60–61,** 1, 2017.
4. Lenselink, E.A. Role of fibronectin in normal wound healing. Int Wound J **12,** 313, 2015.
5. Poujade, M., Grasland-Mongrain, E., Hertzog, A., *et al.* Collective migration of an epithelial monolayer in response to a model wound. Proc Natl Acad Sci U S A **104,** 15988, 2007.
6. Werner, S., Krieg, T., and Smola, H. Keratinocyte-fibroblast interactions in wound healing. J Invest Dermatol **127,** 998, 2007.
7. El Ghalbzouri, A., Hensbergen, P., Gibbs, S., Kempenaar, J., Van Der Schors, R., and Ponec, M. Fibroblasts facilitate re-epithelialization in wounded human skin equivalents. Lab Invest **84,** 102, 2004.

8. Pastar, I., Stojadinovic, O., Yin, N.C., *et al.* Epithelialization in Wound Healing: a Comprehensive Review. Adv Wound Care **3,** 445, 2014.
9. Billingham, R.E., and Russel, P.S. Studies on wound healing, with special reference to the phenomenon of contracture in experimental wounds in rabbits' skin. Ann Surg **144,** 961, 1956.
10. Watts, G. Wound shape and tissue tension in healing. Br J Surg **47,** 555, 1960.
11. Cardinal, M., Eisenbud, D.E., and Armstrong, D.G. Wound shape geometry measurements correlate to eventual wound healing. Wound Repair Regen **17,** 173, 2009.
12. Vedula, S.R.K., Peyret, G., Cheddadi, I., *et al.* Mechanics of epithelial closure over non-adherent environments. Nat Commun **6,** 1, 2015.
13. Ravasio, A., Cheddadi, I., Chen, T., *et al.* Gap geometry dictates epithelial closure efficiency. Nat Commun **6,** 7683, 2015.
14. Martin, P., and Lewis, J. Actin cables and epidermal movement in embryonic wound healing. Nature **360,** 179, 1992.
15. Jacinto, A., Woolner, S., and Martin, P. Dynamic analysis of dorsal closure in Drosophila: from genetics to cell biology. Dev Cell **3,** 9, 2002.
16. Danjo, Y., and Gipson, I.K. Actin ''purse string'' filaments are anchored by E-cadherin-mediated adherens junctions at the leading edge of the epithelial wound, providing coordinated cell movement. J Cell Sci **111,** 3323, 1998.
17. Bidan, C.M., Kommareddy, K.P., Rumpler, M., *et al.* How linear tension converts to curvature: geometric control of bone tissue growth. PLoS One **7,** e36336, 2012.
18. Bidan, C.M., Kommareddy, K.P., Rumpler, M., Kollmannsberger, P., Fratzl, P., and Dunlop, J.W.C. Geometry as a factor for tissue growth: towards shape optimization of tissue engineering scaffolds. Adv Healthc Mater **2,** 186, 2013.
19. Knychala, J., Bouropoulos, N., Catt, C.J., Katsamenis, O.L., Please, C.P., and Sengers, B.G. Pore geometry regulates early stage human bone marrow cell tissue formation and organisation. Ann Biomed Eng **41,** 917, 2013.
20. Ehrig, S., Schamberger, B., Bidan, C.M., *et al.* Surface tension determines tissue shape and growth kinetics. Sci Adv **5,** 1, 2019.
21. Mailand, E., Li, B., Eyckmans, J., Bouklas, N., and Sakar, M.S. Surface and bulk stresses drive morphological changes in fibrous microtissues. Biophys J **117,** 975, 2019.
22. Dehn, R., and Asprey, D. Essential Clinical Procedures, 4th Edition. Philadelphia, PA: Elsevier, 2020.
23. Li, B., and Wang, J.H.C. Fibroblasts and myofibroblasts in wound healing: force generation and measurement. J Tissue Viability **20,** 108, 2011.
24. Schreier, T., Degen, E., and Baschong, W. Fibroblast migration and proliferation during in vitro wound healing - A quantitative comparison between various growth factors and a low molecular weight blood dialyzate used in the clinic to normalize impaired wound healing. Res Exp Med **193,** 195, 1993.
25. Ray, A., Slama, Z.M., Morford, R.K., Madden, S.A., and Provenzano, P.P. Enhanced Directional Migration of Cancer Stem Cells in 3D Aligned Collagen Matrices. Biophys J **112,** 1023, 2017.
26. Dickinson, R.B., Guido, S., and Tranquillo, R.T. Biased cell migration of fibroblasts exhibiting contact guidance in oriented collagen gels. Ann Biomed Eng **22,** 342, 1994.
27. Selman Sakar, M., Eyckmans, J., Pieters, R., Eberli, D., Nelson, B.J., and Chen, C.S. Cellular forces and matrix assembly coordinate fibrous tissue repair. Nat Commun **7,** 1, 2016.
28. Bose, P., Eyckmans, J., Nguyen, T.D., Chen, C.S., and Reich, D.H. Effects of geometry on the mechanics and alignment of three-dimensional engineered microtissues. ACS Biomater Sci Eng **5,** 3843, 2019.
29. Foolen, J., Wunderli, S.L., Loerakker, S., and Snedeker, J.G. Tissue alignment enhances remodeling potential of tendon-derived cells - Lessons from a novel microtissue model of tendon scarring. Matrix Biol **65,** 14, 2018.
30. Legant, W.R., Pathak, A., Yang, M.T., Deshpande, V.S., McMeeking, R.M., and Chen, C.S. Microfabricated tissue gauges to measure and manipulate forces from 3D microtissues. Proc Natl Acad Sci U S A **106,** 10097, 2009.
31. Preibisch, S., Saalfeld, S., and Tomancak, P. Globally optimal stitching of tiled 3D microscopic image acquisitions. Bioinformatics **25,** 1463, 2009.
32. Boudaoud, A., Burian, A., Borowska-Wykręt, D., *et al.* FibrilTool, an ImageJ plug-in to quantify fibrillar structures in raw microscopy images. Nat Protoc **9,** 457, 2014.
33. Alnæs, M.S., Blechta, J., Hake, J., *et al.* The FEniCS Project Version 1.5. Arch Numerical Software **3,** 9, 2015.
34. Logg, A., Mardal K-A, and Wells, G. Automated Solution of Differential Equations by the Finite Element Method. Berlin, Heidelberg: Springer, 2012.
35. Geuzaine, C., and Remacle, J.-F. Gmsh: a 3-D finite element mesh generator with built-in pre- and post-processing facilities. Int J Numer Methods Eng **79,** 1309, 2009.
36. Ambrosi, D., Ateshian, G.A., Arruda, E.M., *et al.* Perspectives on biological growth and remodeling. J Mech Phys Solids **59,** 863, 2011.
37. Van Rossum, G., Guido, and Drake, F.L. Python tutorial. Amsterdam Cent voor Wiskd en Inform **620,** 1995.
38. Harris, C.R., Millman, K.J., van der Walt, S.J., *et al.* Array programming with NumPy. Nature **585,** 357, 2020.
39. Hunter JD. Matplotlib: a 2D Graphics Environment. Comput Sci Eng **9,** 90, 2007.
40. Zordan, M.D., Mill, C.P., Riese, D.J., and Leary, J.F. A high throughput, interactive imaging, bright-field wound healing assay. Cytom Part A **79 A,** 227, 2011.
41. Bao, M., Xie, J., Piruska, A., Hu, X., Huck WTS. Microfabricated Gaps Reveal the Effect of Geometrical Control in Wound Healing. Adv Healthc Mater **10,** 2000630, 2020.
42. Foolen, J., Yamashita, T., and Kollmannsberger, P. Shaping tissues by balancing active forces and geometric constraints. J Phys D Appl Phys **49,** 053001, 2015.
43. Pang, Y., Wang, X., Lee, D., and Greisler, H.P. Dynamic quantitative visualization of single cell alignment and migration and matrix remodeling in 3-D collagen hydrogels under mechanical force. Biomaterials **32,** 3776, 2011.
44. Wang, W.Y., Pearson, A.T., Kutys, M.L., *et al.* Extracellular matrix alignment dictates the organization of focal adhesions and directs uniaxial cell migration. APL Bioeng **2,** 046107, 2018.

45. Fraley, S.I., Wu, P.H., He, L., *et al.* Three-dimensional matrix fiber alignment modulates cell migration and MT1-MMP utility by spatially and temporally directing protrusions. Sci Rep **5,** 1, 2015.
46. Sander, E.A., Barocas, V.H., and Tranquillo, R.T. Initial fiber alignment pattern alters extracellular matrix synthesis in fibroblast-populated fibrin gel cruciforms and correlates with predicted tension. Ann Biomed Eng **39,** 714, 2011.
47. Piotrowski-Daspit, A.S., Nerger, B.A., Wolf, A.E., Sundaresan, S., and Nelson, C.M. Dynamics of tissue-induced alignment of fibrous extracellular matrix. Biophys J **113,** 702, 2017.
48. Eastwood, M., Mudera, V.C., McGrouther, D.A., and Brown, R.A. Effect of precise mechanical loading on fibroblast populated collagen lattices: morphological changes. Cell Motil Cytoskeleton **40,** 13, 1998.
49. Smith, M.L., Gourdon, D., Little, W.C., *et al.* Force-induced unfolding of fibronectin in the extracellular matrix of living cells. PLoS Biol **5,** 2243, 2007.
50. Kubow, K.E., Vukmirovic, R., Zhe, L., *et al.* Mechanical forces regulate the interactions of fibronectin and collagen i in extracellular matrix. Nat Commun **6,** 8026, 2015.

Address correspondence to:
Christopher S. Chen, MD, PhD
Department of Biomedical Engineering
Boston University
610 Commonwealth Avenue
Boston, MA 02215
USA

E-mail: chencs@bu.edu

Jeroen Eyckmans, PhD
Department of Biomedical Engineering
Boston University
610 Commonwealth Avenue
Boston, MA 02215
USA

E-mail: eyckmans@bu.edu

Received: November 3, 2020
Accepted: March 12, 2021
Online Publication Date: May 12, 2021